



## Research paper

# Analysis of an all-terrain tracked robot with innovative suspension system



Angelo Ugenti, Rocco Galati, Giacomo Mantriota\*, Giulio Reina

*Department of Mechanics, Mathematics, and Management, Polytechnic University of Bari, Via Orabona 4, Bari, 70125, Italy*

## ARTICLE INFO

**Keywords:**

All-terrain robots  
Tracked robots  
Passive articulated suspension system  
Robot inverse kinematics

## ABSTRACT

Tracked robots are gaining interest in the current context of off-road mobile robotics, especially in soft-terrain applications, because they offer a large contact area with the ground, which provides better traction than wheels or legs. In this paper, a novel passively articulated tracked robot is introduced. On each side, Polibot features a rubber track wrapped around four independently suspended road wheels, an idler wheel, and the sprocket, and it can adapt to many kinds of terrain. An inverse kinematic model for the proposed architecture is also developed to predict the system configuration given the terrain topography. The analytical model is based on constraint equations and a quasi-static force analysis, and it is validated against results obtained from the real prototype, showing good agreement. It can also be used to evaluate the influence of the many suspension design parameters and operating conditions, proving that it can be a useful tool for the proper setup of the robot.

## 1. Introduction

Off-road mobile robots are now widely used in various applications, including disaster management activities [1], military operations [2], planetary exploration [3], and agriculture [4]. A critical aspect for all these applications is locomotion design and, depending on the specific application, researchers can choose between wheeled, legged, tracked or hybrid robots. The locomotion type for off-road robots is designed according to the required performance in terms of maximum speed, energetic efficiency, and mobility in unstructured environments. In general, wheeled robot excel in speed and energetic efficiency, while legged platforms perform better than the others in unstructured environments [5]. Tracked robots represent a middle point, more efficient than legged robots, and with better mobility than wheeled platforms. For this reason, and thanks to their large contact area with the ground, tracked robots have gained a lot of interest for off-road applications, especially on soft and yielding terrains.

The purpose of this paper is to introduce a novel architecture of an off-road tracked robot named Polibot. The robot is shown in Fig. 1(a) along with a CAD rendering with the main dimensions (Fig. 1(b)). On each side, the robot features a rubber track wrapped around four independently suspended road wheels, an idler wheel, and the sprocket. A modeling tool for the inverse kinematics of the proposed design is also presented that predicts the system configuration given the terrain geometry. The analytical model can be useful as well to evaluate the influence of the many design parameters on the robot behavior.

The paper is organised as follows. The original contributions of the proposed system are described in Section 2 by comparison with existing tracked robots that adopt passive articulated architectures. Section 3 details the experimental prototype of Polibot, while Section 4 presents the analytical model developed to assess the mobility of the proposed architecture. The results obtained from the model are described in Section 5 and validated with the real robot. Section 6 concludes the article with the findings and final considerations of the investigation.

\* Corresponding author.

E-mail address: [giacomo.mantriota@poliba.it](mailto:giacomo.mantriota@poliba.it) (G. Mantriota).

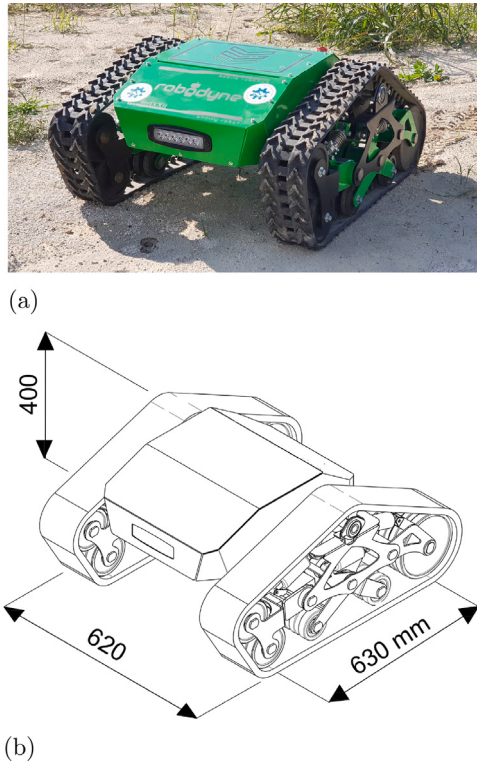


**Fig. 1.** The all-terrain rover Polibot: (a) prototype, and (b) isometric CAD view with the indication of the main dimensions.

## 2. Related research

Tracked locomotion systems can be classified in many different ways. However, considering the body architecture only, tracked robots can have a non-articulated body or an articulated body. The first category includes tracked robots in which the axes of rotation of the road wheels are fixed with respect to the robot frame. This architecture is very widespread among commercial tracked robots. An example is the Trackbot by Inspectorbots [6], a symmetric platform with tracks thicker than the robot body and without external payload that can also operate after a capsize. Another example of a commercial non-articulated tracked robot is provided in [7]. Although non-articulated robots are extremely simple mechanically, they offer poor obstacle negotiation capability.

On the other hand, tracked robots with articulated bodies can be actively articulated, if the degrees of freedom of the body are actuated, or passively articulated, when the degrees of freedom of the body are passive. In general, actively articulated tracked robots are more promising in terms of mobility in unstructured environments [6]. Examples are snakelike robots [8], modular tracked robots [9], hybrid wheel-track robots [10], hybrid leg-track robots [11] and hybrid leg-wheel-track robots [12,13]. However, the mechanical complexity of these designs and the requirement for accurate control of the body usually lead to high manufacturing costs.

Passively articulated tracked robots represent a trade-off between the mechanical simplicity of non-articulated bodies and the mobility of actively articulated platforms. The architecture proposed in this paper and described in Section 3 belongs to this last category.

The simplest passive architecture for tracked rovers usually presents road wheels connected to the body through torsional or linear spring-damper elements of one degree of freedom. For example, Tao et al. [14] developed a stair-climbing tracked robot, in which each side presented four fixed wheels and a suspended wheel with an elastic cushioning device. To improve mobility and obstacle avoidance capabilities, more complex passively articulated tracked designs are required. However, limited work is available in the literature. Kim et al. [15] presented a mobile robot with four independent driving tracks that are connected using two rocker links and four pitch-roll passive joints of two degrees of freedom with the objective of avoiding incomplete contact between the driving tracks and the ground. Sun and Jing [16] proposed a tracked robot with passive bio-inspired suspension, with the objective to improve loading capacity and vibration isolation performance. The bio-inspired suspension is obtained by connecting each loading wheel to an X-shaped structure with springs installed horizontally.

The novelty of the architecture proposed in this paper compared to other existing passively articulated robots is the use of an articulated suspension system, in which each road wheel is suspended independently to adapt to terrain irregularities and distribute pressure evenly in all conditions. The architecture (detailed in Section 3) provides the robot with improved mobility, with lower



Fig. 2. Detailed left side view of Polibot.

mechanical complexity compared to actively articulated robots. The vehicle passive suspension system performs multiple tasks such as maintaining the contact between the rubber tracks and the terrain surface, providing the vehicle stability, and protecting the vehicle frame from all the shocks generated by the terrain unevenness. This is especially important for autonomous off-road robots that carry vision sensors for localisation or data acquisition. A functional comparison between Polibot and an existing robot is presented in Section 5.3. Among the works mentioned above, the suspended tracked vehicle proposed by Sun and Jing [16] is found to be more similar and comparable with the architecture proposed in this work. On the contrary, the robot proposed in [15] is hardly comparable to Polibot, as it comprises four independent tracks, and each track is rigid, meaning that the relative position of the wheels of each track does not change.

The second contribution of this paper consists of the definition of an inverse kinematic model for the proposed architecture using a quasi-static force approach. One of the assets available to mobile robots to achieve autonomous off-road mobility is on-board navigation. An effective kinematic model is necessary to perform real-time computations for autonomous navigation. The literature presents numerous works on the subject. However, very little effort has been made to include suspension kinematics into the model, mainly via computationally expensive multi-body approaches. The reason behind this lack of tracked suspension analytical models is that, unlike wheeled robots [17], tracked rovers usually present mechanically simple suspensions, where the road wheels are fixed to the vehicle frame or connected through torsional or linear spring-damper elements. Galati and Reina [18] proposed an approach to model kinematics for tracked vehicles by obtaining a geometric analogy with a wheeled differential drive model. Sun and Jing [16] proposed a tracked mobile robot with passive bio-inspired suspension, and modeled it via a multi-body software. Ata and Salem [19] adapted the half-car model to tracked vehicles, considering only the pitch and bounce of the vehicle. Guo et al. [20] developed a universal skid steering model based on terramechanics for both wheeled and tracked mobile robots.

A preliminary formulation of the analytical model for Polibot was presented in [21]. Here, a more complete model is developed expressed in a compact and efficient matrix form. The novelty of the proposed model in comparison with the limited related research available is that it is capable, given the shape of the supporting surface, of computing the pose of the rover and the complete configuration of its suspension system considering the constant-length constraint imposed by the presence of the track.

### 3. Polibot

The fully functioning prototype of the all-terrain rover Polibot is shown in Fig. 1(a) along with a CAD rendering with indication of the overall dimensions (Fig. 1(b)). A side view of the real robot is shown in Fig. 2. The name derives from an acronym for Politecnico of Bari's robot. It comprises a central body and two side tracks. A rubber track is wrapped around the drive sprocket ( $W_1$ ), the idler wheel  $W_2$ , and the four ground wheels ( $W_i$ ,  $i = 3, \dots, 6$ ). What is unique about the tracked locomotion system is the presence of an articulated passive suspension system on either side that allows each ground wheel to move independently with respect to the vehicle body providing remarkable adaptability to irregular terrain. Referring to the left track suspension (Fig. 2), a detailed numbered schematic of the system is shown in Fig. 3. The meaning of the numbers is explained in Table 1. One can note that the vehicle's weight is distributed over the contact patch via the four road wheels. Each wheel is suspended with respect to the mid subframe  $SF$ , attached to the robot body and accommodating the drive sprocket  $W_1$ , using a dedicated swing arm and a spring-damper element. For example, the front (FSA) and rear (RSA) swing arm allow, respectively,  $W_3$  and  $W_6$  to rotate about the hinges  $D$  and  $E$  in order to conform to the given terrain geometry. In addition, the two swing arms bringing  $W_4$  and  $W_5$  are hinged in  $F$  to form a middle bogie-like sub-suspension. The track tension can be adjusted by controlling the length of the FSA using a male screw rod and a nut-shaped rotation element. The tension adjustment unit is not visible in Fig. 2. The FSA also brings the idler wheel  $W_2$  forming an attack angle with the road wheel  $W_3$  that facilitates the climb of obstacles.

Polibot is a ROS-based skid steer vehicle equipped with two 350 W 24VDC brush motors, each of which is coupled with an angular gearbox with a ratio  $\tau = 30$ . The tracked undercarriage is made of two track assemblies rigidly attached to the main body frame by two brackets. All powertrain components are installed inside the body frame while the drive sprocket is directly coupled to the gearbox output shaft. The belts are made of fiberglass reinforced bands and an inner steel cord all embedded in melted natural rubber. The drive sprockets and the idle wheels are made of UHMW, which is a high density polyethylene with very high wear resistance. Each belt has a length of about 2000 mm and a width of about 127 mm while the height of the treads is 20 mm placed on a support base having a thickness of 8 mm. It should be noted that the tread height has been designed to be 20 mm to provide better grip on agricultural terrain and to prevent the rubber track from slipping when in contact with soft ground or unpaved surfaces. The sprockets have a total of 17 teeth and a diameter of 200 mm with a thickness of 20 mm and engage the

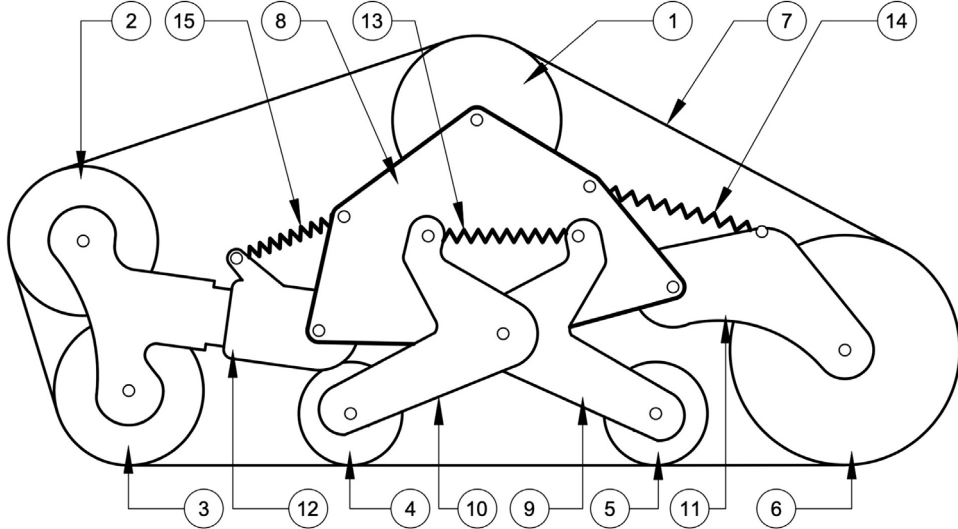


Fig. 3. Suspension components.

**Table 1**  
List of components.

Item number	Description	Symbol
1	Sprocket	$W_1$ (wheel 1)
2	Idler wheel	$W_2$
3	Ground wheel	$W_3$
4	Ground wheel	$W_4$
5	Ground wheel	$W_5$
6	Ground wheel	$W_6$
7	Track	-
8	Subframe	$SF$
9	Bogie rear arm	$BRA$
10	Bogie front arm	$BFA$
11	Rear swing arm	$RSA$
12	Front swing arm	$FSA$
13	spring-damper	$S_1$
14	spring-damper	$S_2$
15	spring-damper	$S_3$

rubber tracks around their bushings that have a pitch of 26 mm to provide traction. In the proposed design, the drive sprocket is placed on top to prevent the power transmission elements to wear out faster due to environmental contamination from dust, mud and granular terrain or get damaged as a result of collisions with rocks and obstacles. This solution partially limits the extension of the wrapping angle. However, attention has been paid that at least three teeth are simultaneously engaged, which guarantee a correct power transmission. To further mitigate system sensitivity to detracking issues, higher teeth have been cut for the sprocket that exceed the rubber belt thickness.

The electronics installed on board the robot integrate current and voltage sensors to measure the power drawn by the motors in addition to two quadrature optical encoders with 1024 pulses that are mounted on the rear shaft of both motors in order to implement a closed-loop speed control. The vehicle has been designed to provide an upper flat surface that can be used to place additional devices and sensors like laptops, LiDARS, IMUs or cameras. Polibot features an embedded industrial computer with Intel i7 CPU, 16 GB RAM DDR and 256 GB SSD providing wireless connectivity with Wi-Fi and Bluetooth interfaces. The main operating system installed on the computer is Ubuntu and it is used to run ROS and to generate locomotion commands over a RS232 serial port directly connected to the motors controller. The main power supply consists of a 24VDC 30Ah LiPo battery package providing 30Ah with an overall standard autonomy of about 3 h.

#### 4. Rover modeling

This section presents the inverse kinematic model that involves computing the pose of the rover and the configuration of its suspension system, given the shape of the supporting surface. To this aim, a contact model must be first defined. For tracked vehicles, a contact model may be difficult to define. In first approximation, it is assumed that the track has negligible thickness and conforms perfectly to the terrain geometry. Then each road wheel is in contact with the supporting surface at its lowest point,

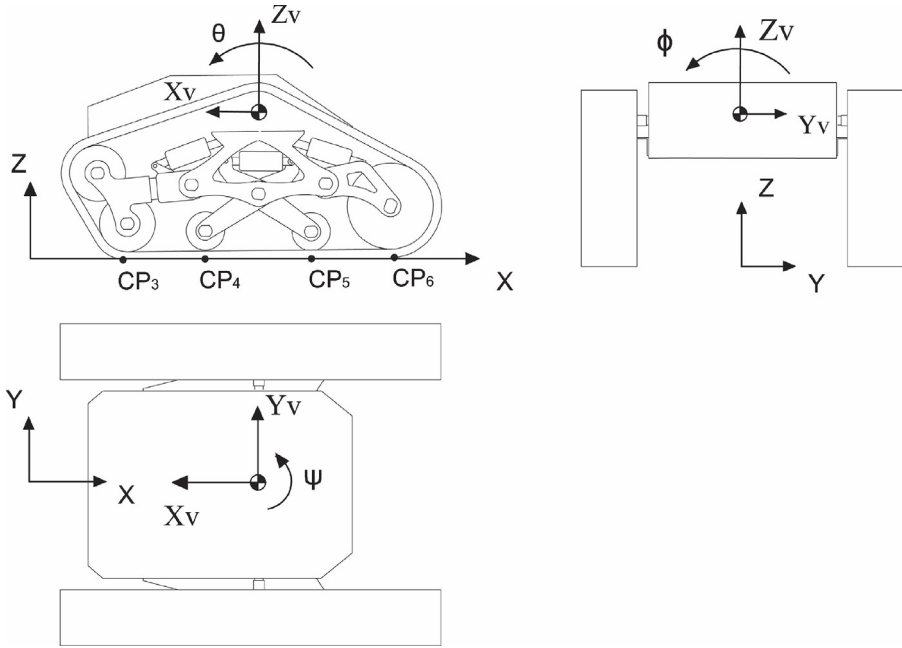


Fig. 4. Polibot coordinate frames.

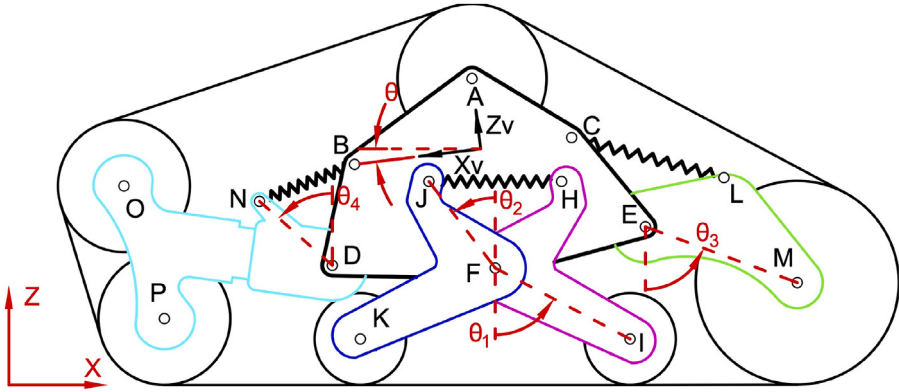


Fig. 5. Left suspension schematics.

denoted by  $CP_i, i = 3, \dots, 6$  to match the numbering of the road wheel, as explained in Fig. 4. This is a reasonable assumption when moving over firm terrain. For vehicles moving on soft terrain, distributed track-terrain contact stresses should be considered and resolved to resultant forces at a single point. In the case of negotiation of a rock, the contact point depends on the obstacle geometry and can be defined referring to the wheel-terrain contact plane, as detailed, for example, in [17].

The input to the analytical model is the geometric properties of the robot and the elevation map of the terrain. The outputs are the position and tilt of the vehicle body (i.e., mid subframe  $SF$ ) along with the suspension configuration.

In the remainder of this Section, the Polibot model is developed as follows: Section 4.1 deals with the degrees of freedom of the system, while Sections 4.2 and 4.3 describe the equations required to solve the inverse kinematic problem.

#### 4.1. Degrees of freedom

By referring again to the left suspension of Polibot (Fig. 3), and considering only the points of the rigid bodies that interact with other components, the system can be further schematised as shown in Fig. 5. For clarification, the rigid bodies that compose the kinematic scheme (wheels and spring excluded) are listed in Table 2, and their geometry is detailed in Appendix A. It is important to highlight that the dimension  $d_{11}$  (shown in Fig. A.1 in Appendix A) can be changed by the tension adjustment unit and therefore it is considered as an input parameter.

**Table 2**  
List of rigid bodies.

Body number	Points	Color
1	ABDFEC	Black
2	HFI	Magenta
3	JFK	Blue
4	ELM	Green
5	DNOSP	Cyan

**Table 3**  
List of degrees of freedom as shown in Fig. 5.

Number	Symbol	Description
1	$X_A$	SF vertical position
2	$Z_A$	SF horizontal position
3	$\theta$	SF Pitch
4	$\theta_1$	BRA orientation
5	$\theta_2$	BFA orientation
6	$\theta_3$	RSA orientation
7	$\theta_4$	FSA orientation

To study the motion of the suspension system, a global reference frame  $XYZ$  is defined in Fig. 4. Please note that for simplicity sake, a half-symmetry model is assumed, i.e., the vehicle center of mass is constrained to the  $X - Z$  plane and the chassis can only pitch ( $\theta$ ) whereas roll and yaw rotations ( $\phi$  and  $\psi$ ) are not taken into account.

Under this assumption, the system of Fig. 5 consists of five rigid bodies connected by three revolute joints (D, E, F). The seven resulting degrees of freedom are listed in Table 3.

#### 4.2. Constraints

The terrain elevation map that is assumed to be known in this analysis can be represented by the following expression:

$$Z = f_{te}(X) \quad (1)$$

where  $f_{te}$  is the terrain elevation function, that gives the height of the terrain ( $Z$ ) for any value of  $X$ . For example, the terrain elevation function for a flat horizontal surface is  $Z = h_0$ , with  $h_0$  a constant.

Referring to Fig. 5, given the  $X$ -coordinate of the first contact point  $X_{CP_3}$  and assuming that wheels 3 to 6 make contact with the ground with their lowest point, the following constraint equations can be written:

$$X_P = X_{CP_3} \quad (2)$$

$$Z_P - r_3 = f_{te}(X_P) \quad (3)$$

$$Z_K - r_4 = f_{te}(X_K) \quad (4)$$

$$Z_I - r_5 = f_{te}(X_I) \quad (5)$$

$$Z_M - r_6 = f_{te}(X_M) \quad (6)$$

where  $r_i$  is the radius of wheel  $i$ . Given the geometry of the suspension (please refer to Fig. A.1 in Appendix A), the  $Z$ -coordinate of the wheel centers (P, K, I and M) can be expressed as a function of the degrees of freedom of Table 3 via loop closure equations. For conciseness, these expressions are omitted here and reported in Appendix B.

Another constraint equation is derived from the adoption of a steel-core rubber track, whose length can be considered reasonably constant, thus imposing the following geometric condition that must be satisfied during the relative motion of the suspension elements:

$$L_{track} = L_{nom} \quad (7)$$

where  $L_{nom}$  is the nominal length of the track. The derivation of  $L_{track}$  as a function of the degrees of freedom is reported in Appendix D.

The system of non linear equations (2)–(7) consist of six equations in seven unknowns, which are the seven degrees of freedom. Thus, at this stage the inverse kinematic problem is under constrained and there exists an infinite set of solutions. For this reason, it is necessary to consider the quasi-static equilibrium equations, as explained in the next section.

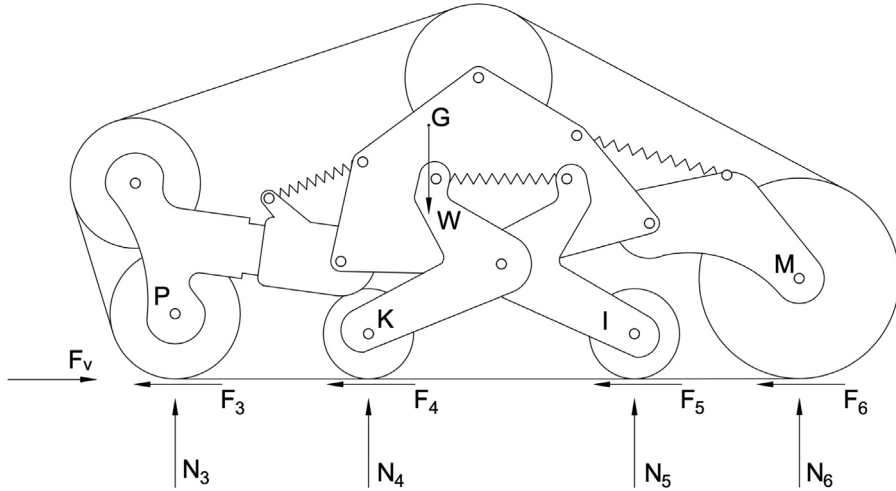


Fig. 6. Global free body diagram of Polibot.

#### 4.3. Quasi-static analysis

If a vehicle has more than two contact points as Polibot, it will be dynamically indeterminate and the normal forces under the wheels cannot be obtained by global equilibrium equations. For these two reasons it is necessary to consider the elastic element deflection. To do so, the equilibrium of moments acting on the BRA, BFA, RSA and FSA around joints D, F and E should be added to the problem. The rover's weight and the position of the center of gravity in the vehicle coordinate frame ( $Xv_G$ ,  $Zv_G$ ) have been experimentally estimated with the use of scales.

The robot is assumed to move at a constant speed, therefore the only external forces acting in the longitudinal direction are the tangential forces under each wheel ( $F_i$ , for  $i = 3, \dots, 6$ ) and the motion resistance of the running gear ( $F_v$ ), as indicated in Fig. 6. The motion resistance of the running gear accounts for obstacle resistance, internal resistance of the running gear and the resistance due to interaction with the terrain.

The required equilibrium equations can be easily derived from Figs. 6 and 7 and they can be written in matrix form as follows:

$$\begin{bmatrix}
 1 & 0 & 1 & 0 & 1 & 0 & 1 & 0 \\
 0 & 1 & 0 & 1 & 0 & 1 & 0 & 1 \\
 0 & CP_3^x & 0 & CP_4^x & 0 & CP_5^x & 0 & CP_6^x \\
 0 & CP_3^x - X_D & 0 & 0 & 0 & 0 & 0 & 0 \\
 0 & 0 & 0 & CP_4^x - X_F & 0 & 0 & 0 & 0 \\
 0 & 0 & 0 & 0 & CP_5^x - X_F & 0 & 0 & 0 \\
 0 & 0 & 0 & 0 & 0 & CP_6^x - X_E & 0 & 0 \\
 1 & 0 & 1 & 0 & 1 & 0 & 1 & 0 \\
 1 & -k_c & 0 & 0 & 0 & 0 & 0 & 0 \\
 0 & 0 & 1 & -k_c & 0 & 0 & 0 & 0 \\
 0 & 0 & 0 & 1 & -k_c & 0 & 0 & 0 \\
 0 & 0 & 0 & 0 & 0 & 1 & -k_c & 0
 \end{bmatrix} \cdot \begin{bmatrix} F_3 \\ N_3 \\ F_4 \\ N_4 \\ F_5 \\ N_5 \\ F_6 \\ N_6 \end{bmatrix} + \begin{bmatrix} 0 & 0 & 0 & 0 & 0 \\ 0 & 0 & 0 & 0 & 0 \\ 0 & 0 & 0 & 0 & 0 \\ 0 & CP_3^z - Z_D - a & 0 & 0 & b \\ 0 & 0 & Z_J - Z_F & 0 & 0 \\ 0 & 0 & Z_F - Z_H & 0 & 0 \\ Z_E - CP_6^z + c & 0 & 0 & d & 0 \\ 1 & -1 & 0 & 0 & 0 \\ 0 & 0 & 0 & 0 & 0 \\ 0 & 0 & 0 & 0 & 0 \\ 0 & 0 & 0 & 0 & 0 \end{bmatrix} \cdot \begin{bmatrix} F_v \\ W \\ T_1 \\ T_2 \\ F_{el,1} \\ F_{el,2} \\ F_{el,3} \end{bmatrix} = \begin{bmatrix} F_3 \\ N_3 \\ F_4 \\ N_4 \\ F_5 \\ N_5 \\ F_6 \\ N_6 \\ 0 \\ 0 \\ 0 \\ 0 \\ 0 \\ 0 \\ 0 \\ 0 \end{bmatrix} \quad (8)$$

which in compact form can be written as follows:

$$G_c \cdot f_c + G_{int} \cdot f_{int} = f_s \quad (9)$$

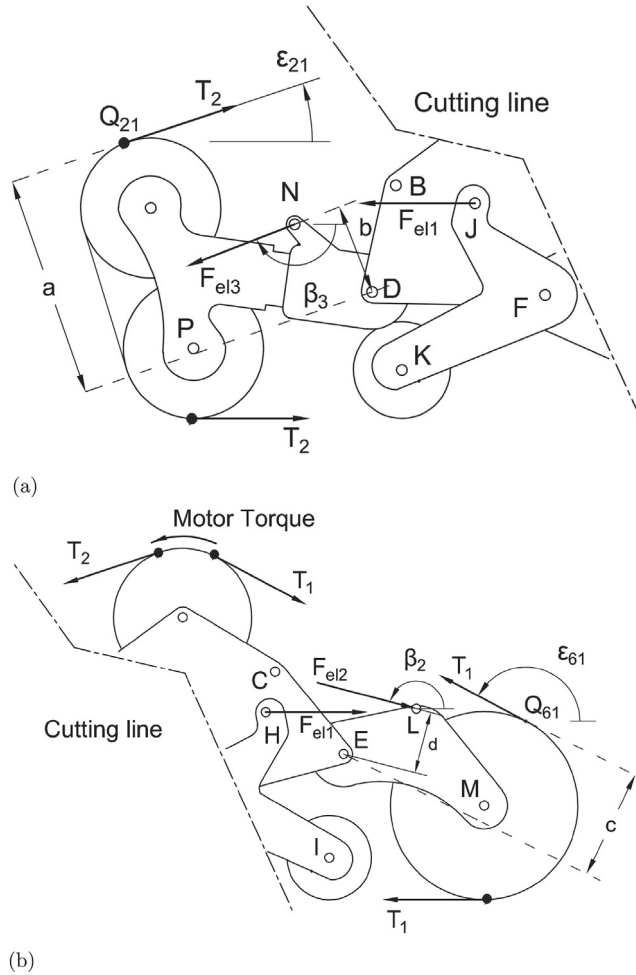


Fig. 7. Internal forces acting on Polibot suspension system: left half (a), right half (b).

where  $f_c$  includes all the forces arising from wheel-ground interaction (i.e. normal and tangential forces),  $f_{int}$  represents the internal forces (i.e. track tension and elastic forces),  $f_s$  includes the summed effects of gravitational forces, inertial forces, and forces due to interaction with the environment. The geometric parameters  $a$ ,  $b$ ,  $c$  and  $d$  are indicated in Fig. 7. The system (9) consists in a set of 12 equations in 14 unknowns. The twelve equations include, in order:

- global force balance along X
- global force balance along Z
- global torque balance around the center of gravity
- torque balance on BRA around point F
- torque balance on BFA around point F
- torque balance on RSA around point E
- torque balance on FSA around point D
- longitudinal force balance of the track element that exchanges forces with the ground
- proportionality between  $F_i$  and  $N_i$ , one equation per wheel (i.e. for  $i = 3, \dots, 6$ )

The last four equations (proportionality between  $F_i$  and  $N_i$ ) are required to distribute the tractive effort to each wheel proportionally to the terrain normal reaction.

The 14 unknown parameters are described in Table 4, and they also include the proportionality constant between tangential and normal wheel-terrain forces  $k_c$  defined as follows:

$$k_c = \frac{F_i}{N_i}, \quad \text{for } i = 3, \dots, 6 \quad (10)$$

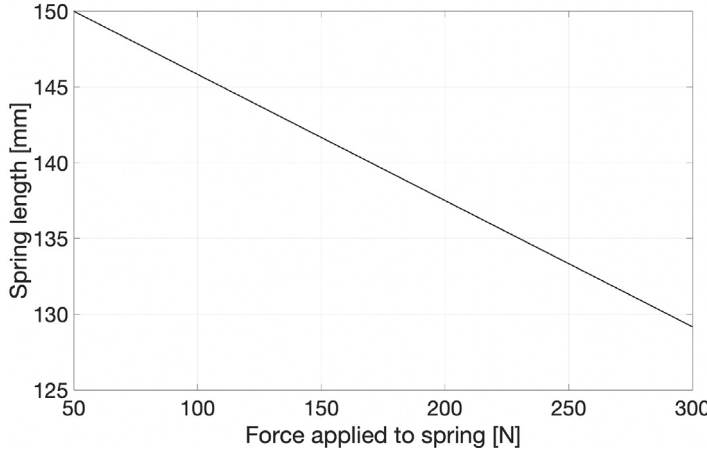


Fig. 8. Force-length characteristic of a spring with 12 N/mm stiffness, 50 N pre-load, and maximum length of 150 mm.

**Table 4**  
List of force parameters.

Unknown force	Description
$T_1$	Tension of the track, tight side
$T_2$	Tension of the track, slack side
$F_3$	Tangential traction force for $W_3$
$F_4$	Tangential traction force for $W_4$
$F_5$	Tangential traction force for $W_5$
$F_6$	Tangential traction force for $W_6$
$N_3$	Normal reaction force for $W_3$
$N_4$	Normal reaction force for $W_4$
$N_5$	Normal reaction force for $W_5$
$N_6$	Normal reaction force for $W_6$
$k_c$	Proportionality constant between $F_i$ and $N_i$
$F_{el,1}$	Force applied to $S_1$
$F_{el,2}$	Force applied to $S_2$
$F_{el,3}$	Force applied to $S_3$

To close the system of equations, it is necessary to consider the deflection of the elastic elements. Each spring has a pre-load and behaves as a rigid body if any force lower than the pre-load is applied. For example, the force-length characteristic of a spring with stiffness 12 N/mm, pre-load 50 N and maximum length 150 mm is shown in Fig. 8, where the force applied to the spring is considered in compression. If a traction force is applied to the spring, the elastic element behaves as a rigid body and the length is equal to its maximum length. This characteristic can be generalised and applied to the three elastic elements of the suspension:

$$L_i = \begin{cases} L_{max,i}, & \text{if } F_{el,i} < F_{pre,i} \\ L_{max,i} - \frac{F_{el,i} - F_{pre,i}}{k}, & \text{otherwise} \end{cases} \quad i = 1, 2, 3 \quad (11)$$

where  $L_i$  is the length of spring  $i$  when a force  $F_{el,i}$  is applied to its ends,  $F_{pre,i}$  and  $L_{max,i}$  are the pre-load and the maximum length of spring  $i$  respectively,  $k$  is the elastic stiffness. The length of the elastic elements ( $L_i$  for  $i = 1, 2, 3$ ) is derived as a function of the degrees of freedom in Appendix C. Pre-loads and maximum lengths are input parameters.

The system of equations (9) and (11) consists of 15 equations in 14 unknowns. However, it cannot be solved independently of the constraint equations shown in Section 4.2. In fact, the matrices  $G_c$  and  $G_{int}$  are functions of the seven degrees of freedom of the system, as shown in Appendix E. For these reasons, the force analysis conducted in this section must be coupled with the constraint equations (2)–(7), resulting in a system of 21 equations in 21 unknowns. The unknowns are the seven degrees of freedom of Table 3 plus the fourteen unknown parameters of Table 4.

## 5. Results and discussion

### 5.1. Model validation

The ability of the proposed model to predict the configuration of the real Polibot is evaluated in various scenarios. First, the static or baseline configuration of Polibot is considered. Then, the influence of the weight change on the system configuration is investigated. Finally, two conditions of obstacle climb are evaluated. In all tests, the robot configuration as predicted by the quasi-static kinematic model is compared with that of the real prototype.

**Table 5**  
Input parameters for the static configuration.

Parameter	Description	Value
$X_{CP_3}$	X-coordinate of contact point for $W_3$	0
$f_{te}$	Terrain elevation function	Z = 0
$L_{nom}$	Nominal track length	2026 mm
$m_{nom}$	Robot's mass	96.2 kg
$(X_G^v, Z_G^v)$	Center of gravity in vehicle coordinates	(50, -100) mm
$F_{res}$	Motion resistance	0 N
$L_{max,1}$	Maximum length of spring 1	150 mm
$L_{max,2}$	Maximum length of spring 2	150 mm
$L_{max,3}$	Maximum length of spring 3	130 mm
$F_{pre,1}$	Pre-load of spring 1	60 N
$F_{pre,2}$	Pre-load of spring 2	0 N
$F_{pre,3}$	Pre-load of spring 3	120 N
$d_{11}$	Length of FSA (Fig. A.1)	198 mm

**Table 6**  
Polibot configuration expressed in the global reference frame as obtained from the quasi-static model and measured from the real robot in the static configuration.

Variable	Analytical model	Real robot	Relative error [%]
$X_A$ [mm]	311.0	303.9	2.3
$Z_A$ [mm]	303.3	309.4	-1.9
$\theta$ [deg]	4.41	4.02	10.0
$\theta_1$ [deg]	61.6	59.1	4.3
$\theta_2$ [deg]	38.3	40.8	-6.1
$\theta_3$ [deg]	71.6	72.2	-0.9
$\theta_4$ [deg]	52.2	53.5	-2.5

**Table 7**  
Results of 80 kg payload configuration.

Configuration	Variable	Analytical model	Measurement	Relative error [%]
Added mass (80 kg)	$Z_A$ [mm]	291.2	300.5	-3.1
	$\theta$ [deg]	2.61	3.04	-13.3

### 5.1.1. Static configuration and impact of payload

The static or baseline configuration refers to the robot at rest on a flat surface (see, for example, Fig. 2). The actual robot parameters are used in the analytical model, as shown in Table 5.

The results obtained from the analytical model compared with the experimental measurements taken manually using a measuring tape and a digital inclinometer are collated in Table 6. The average relative percentage error in predicting the real robot configuration resulted in about 4% with a worst case scenario of 10% for the chassis pitch angle estimation.

It should be noted that a nominal pitch angle is required for the system: the payload will be added to the robot in such a way that the chassis will tend to rotate clockwise. In addition, a positive nodding angle is sought to keep the line of sight and look-ahead distance in a range of about 1–3 meters away from the robot. Therefore, a positive pitch angle is generally considered positive and a requirement of the robot.

When the robot weight increases by 83% simulating the addition of a 80 kg payload, all suspension elements are compressed, leading to a decrease of the center of mass height of 12 mm and a rotation of the chassis of 1 degree, as shown in Fig. 9. The comparison of the analytical model with the real robot configuration is reported in Table 7. Again, the largest error results in the pitch angle prediction (13%), whereas the center of mass height is estimated with a 3% accuracy.

### 5.1.2. Obstacle negotiation

Two configurations are evaluated for the case of a 55-millimeter-high obstacle below the front and rear wheels respectively. The comparison between simulated and real suspension for each of these scenarios is shown in Fig. 10, and the numerical results are collected in Table 8. When the robot is negotiating the obstacle with its front wheel, the chassis rotates clockwise, resulting in a negative pitch angle (-2.98 deg). When the obstacle is moved below  $W_6$ , the pitch angle increases of 3.3 degrees when compared to the baseline static configuration. In both cases, the error in the estimation of the pitch angle via the analytical model is not higher than 10%, while the maximum error for the center of gravity height is 3%.

To further validate the model, a second obstacle negotiation scenario is considered, in which the robot negotiates a vertical wall. The real robot is commanded to move against a wall, Fig. 11 (b), and the manoeuvre is stopped at different checkpoints to take manual measurements used for comparison with the model. The results are shown in Fig. 12, where the simulated and real robot pitch is plotted against the vertical displacement of the idler wheel ( $W_2$ ) along the wall. Each black dot represents a measurement checkpoint during the experiment. For safety reasons, the experiment is stopped when the pitch angle reaches -40 degrees, to avoid

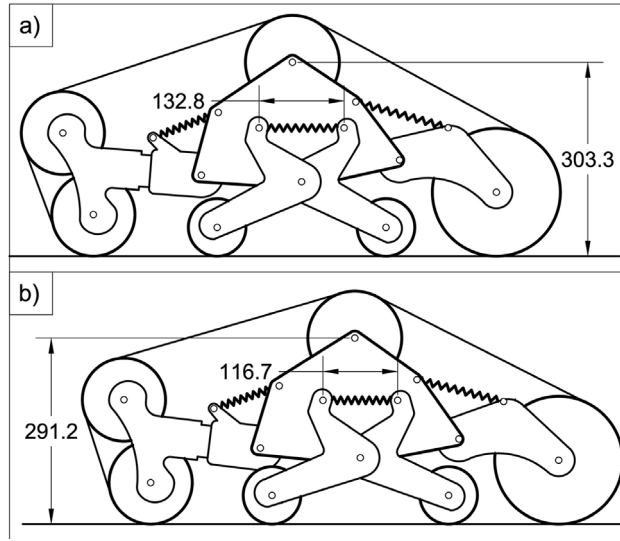


**Fig. 9.** Comparison of baseline (a) and 80 kg payload (b) configurations.

**Table 8**  
Results of obstacle negotiation configurations.

Configuration	Variable	Analytical model	Measurement	Relative error [%]
Obstacle $W_3$ (55 mm)	$Z_A$ [mm]	307.9	318	-3.2
	$\theta$ [deg]	-2.69	-2.98	10.0
Obstacle $W_6$ (55 mm)	$Z_A$ [mm]	307.8	313	-1.7
	$\theta$ [deg]	7.31	8.07	-8.8

damage to the prototype. The simulation, however, carries on up to almost -90 degrees, where the only wheel in contact with the ground is the rear road wheel ( $W_6$ ) and the simulated robot is about to turn over. In the range covered by the experiments, the average relative error between the simulated and measured pitch angle is 4.7%.

## 5.2. Polibot setup analysis

Once the model has been validated, it can be used in a number of ways. For example, to analyze the system behavior in the neighborhood of the baseline configuration. In this context, three Key Performance Indicators (KPIs) are defined in this work and listed in [Table 9](#). The first KPI is the pitch of the robot  $\theta$ . It can be considered as a performance indicator because the objective of a suspension is to keep the sprung mass stable and as close as possible to its initial configuration. Moreover, a mobile robot might carry instrumentation for data collection that need the robot frame to be aligned with the gravity field. The second and third KPI are related to the capability of the suspension to distribute the robot's weight across the four ground wheels. The KPI indicated with  $n_{cont}$  represents the number of wheels that make contact with the ground simultaneously. This is an important parameter to evaluate, because the suspension implemented in Polibot was designed to guarantee contact with the ground for all four road wheels to improve traction performance on all kind of terrains. Ideally,  $n_{cont}$  should always be equal to 4, but changes in design parameters or operating conditions can cause it to drop to 3. Finally, the third KPI ( $\sigma_N$ ) is the normalised standard deviation of ground normal forces. A low value of  $\sigma_N$  indicates that the weight of the robot is well distributed across the four road wheels, with beneficial effects in terms of lower terrain compaction and better traction. This final KPI can be computed as follows:

$$\sigma_N = \frac{\sqrt{\frac{1}{4} \sum_{i=3}^6 (N_i - \bar{N})^2}}{\bar{N}} \quad (12)$$

with:

$$\bar{N} = \frac{1}{4} \sum_{i=1}^4 N_i \quad (13)$$

where  $N_i$  ( $i = 3, \dots, 6$ ) is the normal reaction force below each road wheel.

First, the effect of adding mass to the system is analyzed, assuming that the position of the center of gravity is not affected. The results are shown in [Fig. 13](#). As the robot mass increases, the pitch ( $\theta$ ) decreases slightly. For example, an increase of 20% in robot mass causes a reduction of only half a degree in pitch angle. This result is important for the repeatability of the experiments,

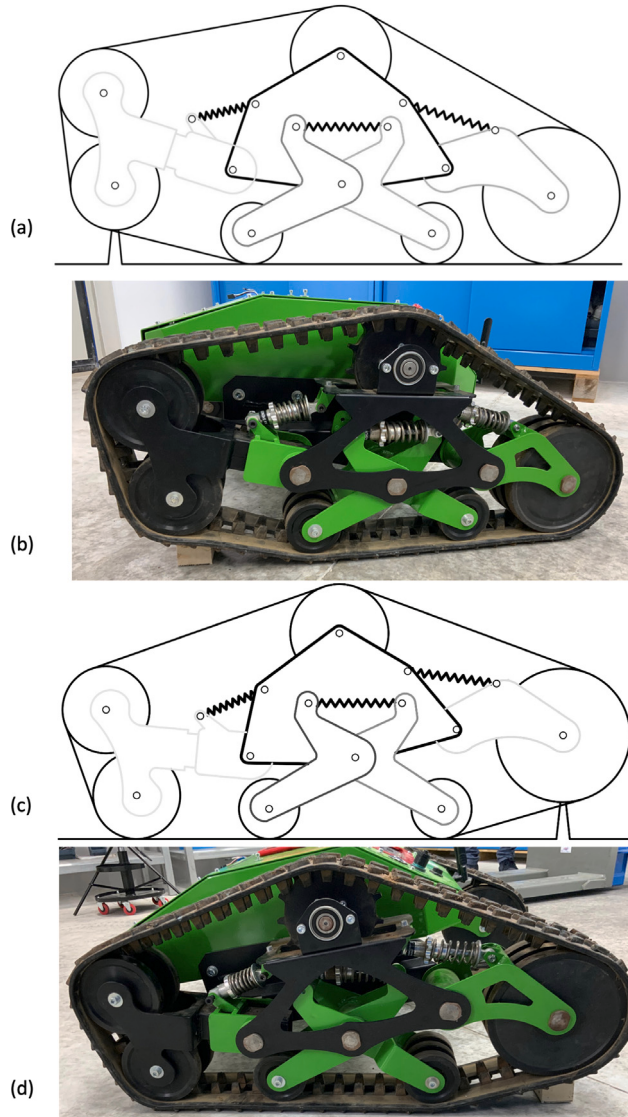


**Fig. 10.** Comparison between simulated (a) and real (b) obstacle negotiation for the front wheel  $W_3$  and between simulated (c) and real (d) obstacle negotiation for the rear wheel  $W_6$ . The obstacle is 55-mm high in all cases.

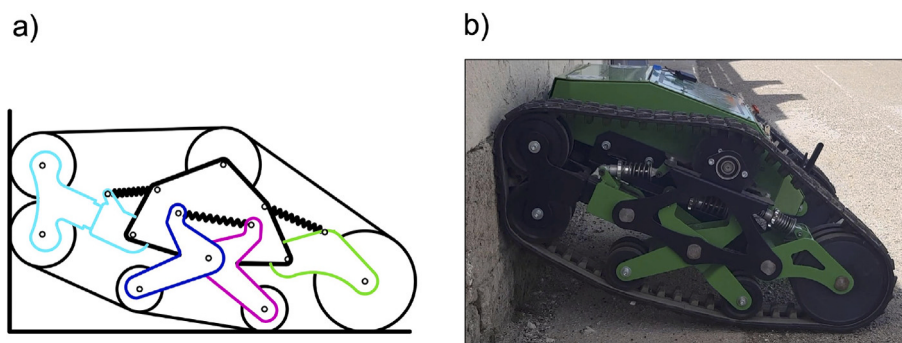


**Fig. 11.** Comparison between the analytical model (a) and the real robot (b) in a wall climbing scenario.

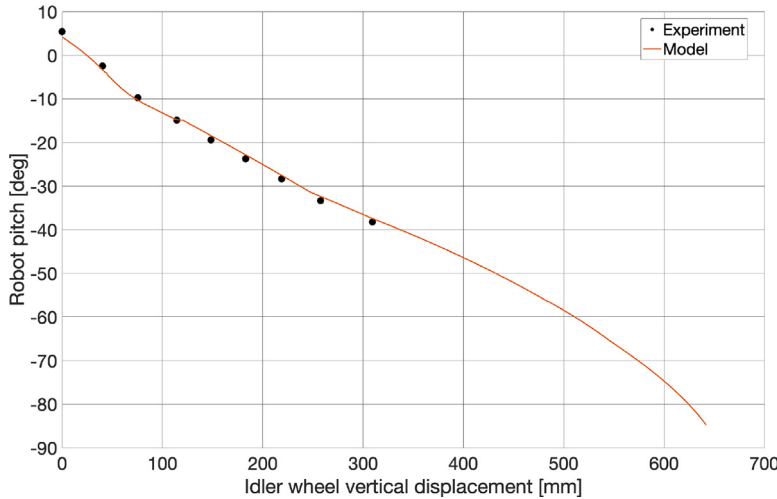


**Fig. 12.** Robot pitch as a function of the vertical displacement of the idler wheel ( $W_2$ ) in a wall climbing scenario: experimental measurements taken from the real robot (black dots) compared with the analytical model (red line). (For interpretation of the references to color in this figure legend, the reader is referred to the web version of this article.)

**Table 9**  
Key Performance Indicators.

KPI	Description
$\theta$	Robot pitch
$n_{cont}$	Number of wheels that make contact with the ground
$\sigma_N$	Normalised standard deviation of ground normal forces

because the look-ahead distance of exteroceptive sensors will not be influenced by fluctuations of the robot mass that can be caused by different test setups. However, although all four wheels are always in contact with the ground,  $N_{std}$  initially increases with the robot mass, reaches a maximum, and then starts to decrease. This can be explained by the middle elastic element being more affected by the reduced robot body height associated with the increase in mass. An increase in robot mass also causes a reduction of track tension, as shown in Fig. 14. For a robot mass 65% higher than the baseline value, the track tension drops almost to zero, which is detrimental for traction. However, in this case, the track tension can be brought back up with the tension adjustment unit, as explained in the remainder of this section.

Two other strictly related design parameters are analyzed in this section: the track length ( $L_{nom}$ ) and the length of the Front Swing Arm, indicated with  $d_{11}$  (as show in Fig. A.1 in Appendix A). The length of the FSA can be changed by the tension adjustment unit. A reduction of track length and an increase in FSA length have the same common effect to increase the tension of the track, as shown in Figs. 15 and 16. Usually, the track tension is adjusted to the minimum possible to avoid power loss due to friction. However, in off-road applications the track tension should be high enough to maximise the tractive force. The baseline values of  $d_{11}$  and  $L_{nom}$  for Polibot are chosen to achieve an even weight distribution across the road wheels while keeping an adequate level of tension. Figs. 17 and 18 shows the effect on the KPIs of changing track length and FSA length, respectively. As expected, the behavior of the KPIs when increasing the track length is the same obtained by reducing the length of the FSA:  $N_{std}$  decreases, indicating a more uniform distribution of the normal forces below the road wheels. However, this benefit comes to the cost of reducing the track tension (Figs. 15 and 16), which affects the performance of the vehicle. On the other hand, reducing the track length (or increasing the length of the FSA) has the negative effect of a less uniform weight distribution across the four road wheels. When the track length is reduced by 0.15% (or the length of the FSA increased by 0.7%) the rear wheel ( $W_6$ ) is lifted from the ground due to the increased track tension, making  $n_{cont}$  drop from 4 to 3.

### 5.3. Comparison with existing platforms

In this section, the robot proposed in [16] is considered for comparison. The suspension schematic using a bio-inspired X-shaped architecture is shown in Fig. 19(a) along with the corresponding kinematically equivalent model (Fig. 19(b)). For a fair comparison, the distance between the first and last road wheel is set to 630 mm (to match Polibot longitudinal wheelbase) and the radius of all wheels is assumed equal to the radius of Polibot first road wheel. In addition, the parameters of the springs and the track length are chosen to match Polibot initial track tension. Both types of suspension adopt an equal constant-length tensioner. The analytical model for the X-shaped suspension is discussed in Appendix F.

The two suspensions are compared in a scenario of obstacle negotiation. A step-like object is positioned below the first road wheel and its height is changed from zero to 65 mm (equal to the wheel radius). The results in terms of KPIs are shown in Fig. 20.

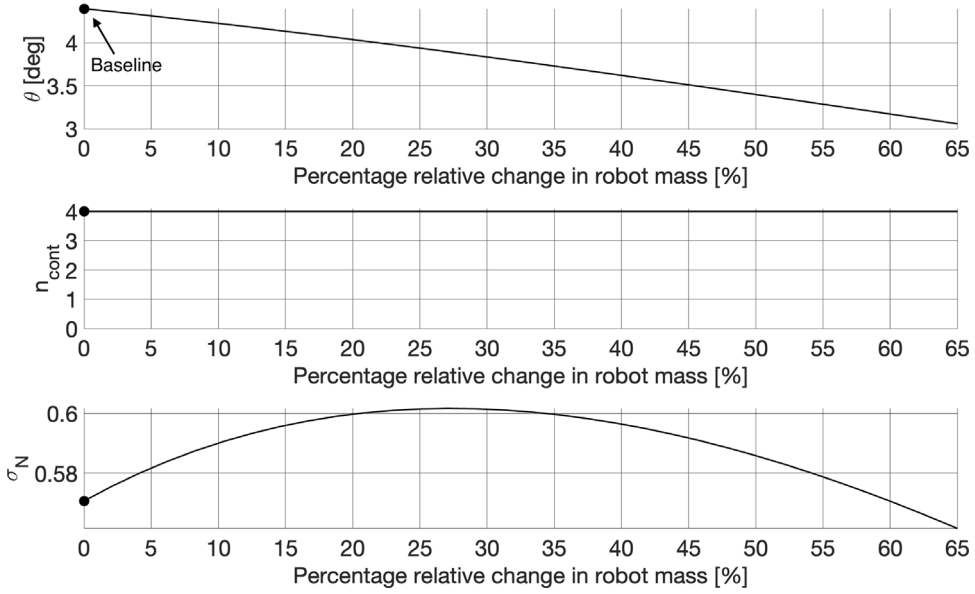


**Fig. 13.** Effect of robot mass on KPIs: robot pitch (top), number of wheels in contact with ground (middle) and normalised standard deviation of ground normal forces (bottom).

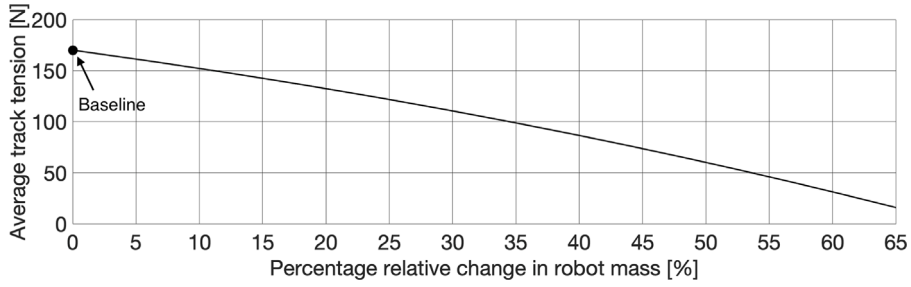


**Fig. 14.** Effect of robot mass on track tension.

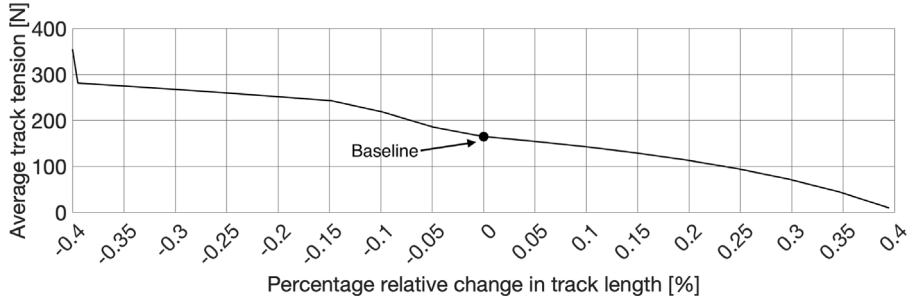


**Fig. 15.** Effect of track length on track tension.

As seen from this figure, the black dashed curves that represent the response of the X-shaped robot interrupt when the step height reaches approximately 35% of the wheel radius. This is because the track tension nulls out at that point, as shown in Fig. 21. Conversely, the tension in Polibot track is well above zero, even when overcoming an obstacle whose height matches the size of the radius of the first road wheel. Referring again to the KPIs of Fig. 20, it can be noted in the middle graph ( $n_{cont}$ ) that Polibot is able to keep all four wheels pushed against the ground, even for high obstacles. This is also visible in the bottom graph that shows how the two architectures distribute the vertical forces acting on the road wheels. For low obstacles (lower than about 28% of the wheel radius) the X-shaped suspension performs better, with a lower  $\sigma_N$ . However, for more challenging and higher obstacles, Polibot outperforms its counterpart.

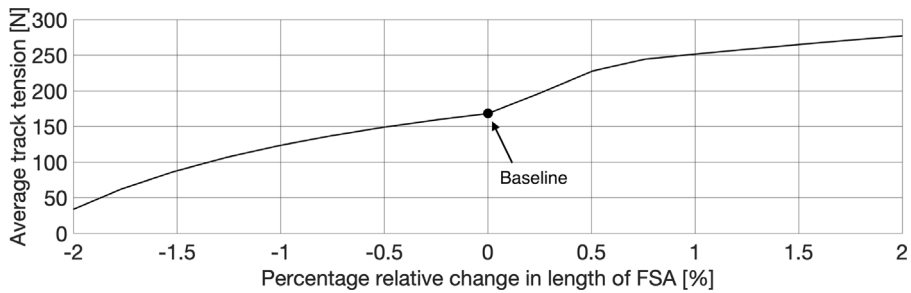


Fig. 16. Effect of FSA length on track tension.

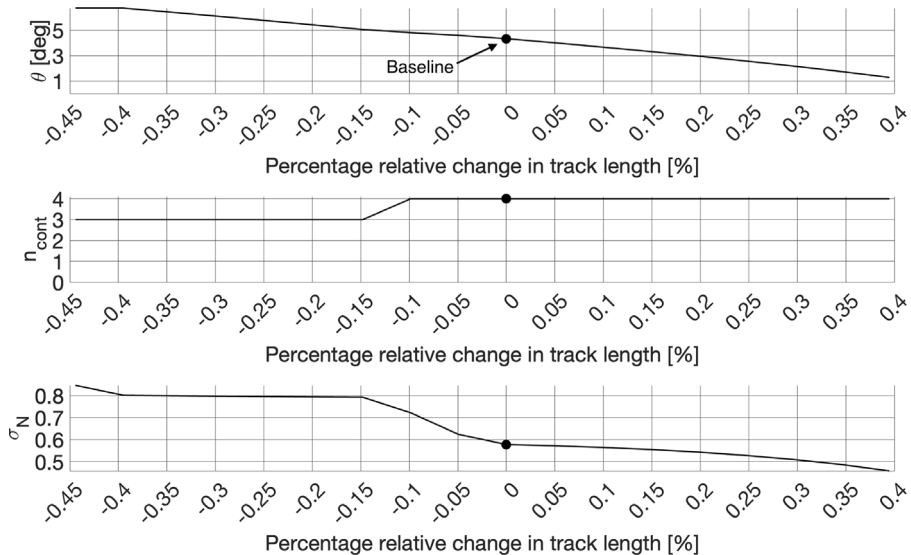


Fig. 17. Effect of track length on KPIs: robot pitch (top), number of wheels in contact with ground (middle) and normalised standard deviation of ground normal forces (bottom).

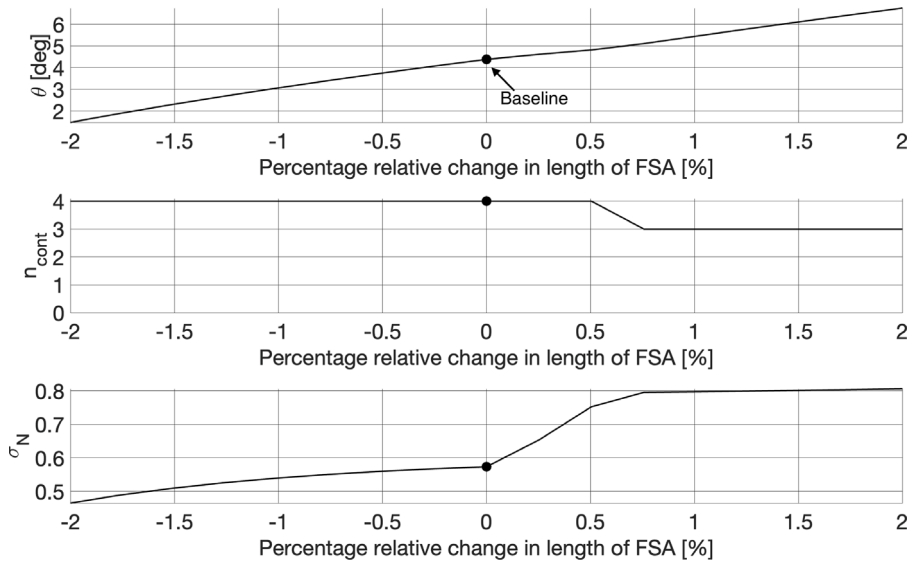
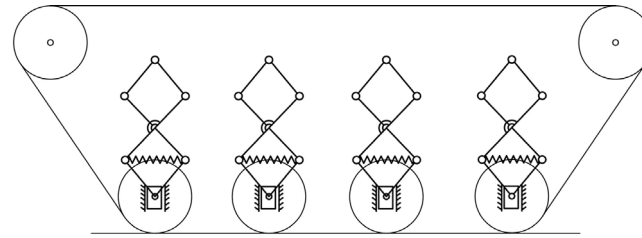
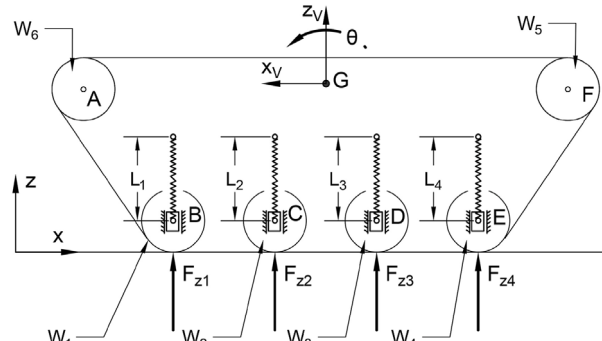


Fig. 18. Effect of FSA length on KPIs: robot pitch (top), number of wheels in contact with ground (middle) and normalised standard deviation of ground normal forces (bottom).



(a)



(b)

**Fig. 19.** The existing X-shaped passive suspension proposed in [16] and compared with Polibot: (a) original scheme, (b) kinematically equivalent model.

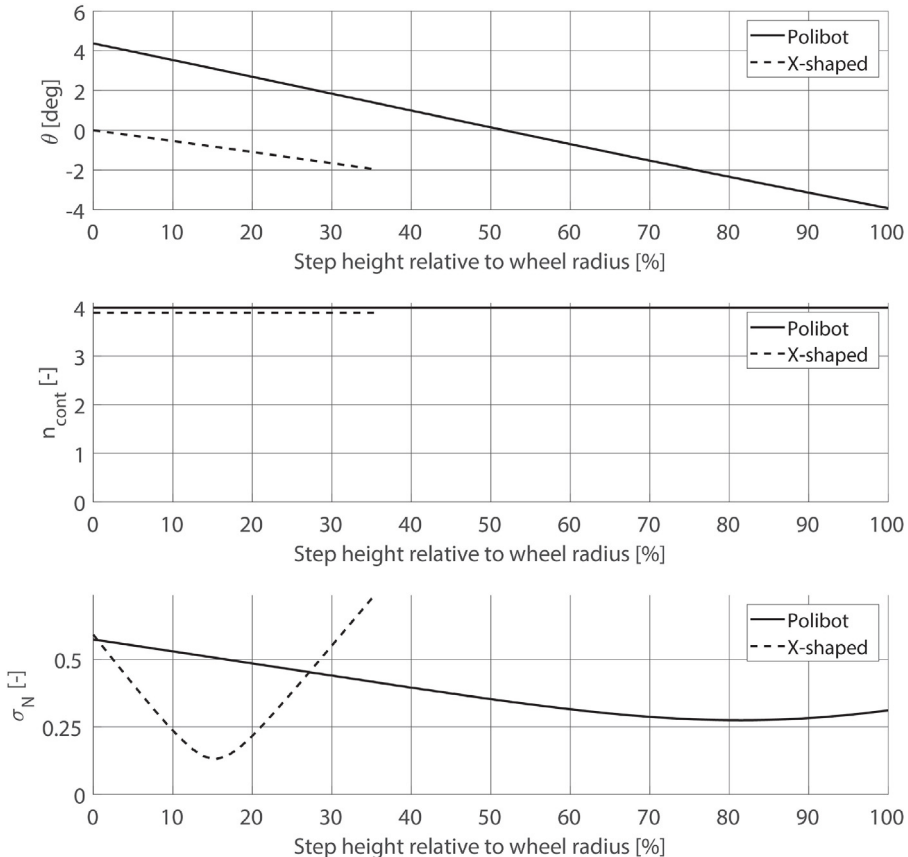


**Fig. 20.** Effect of obstacle height below the first road wheel on KPIs: Polibot (black line) and X-shaped robot (black dashed line).

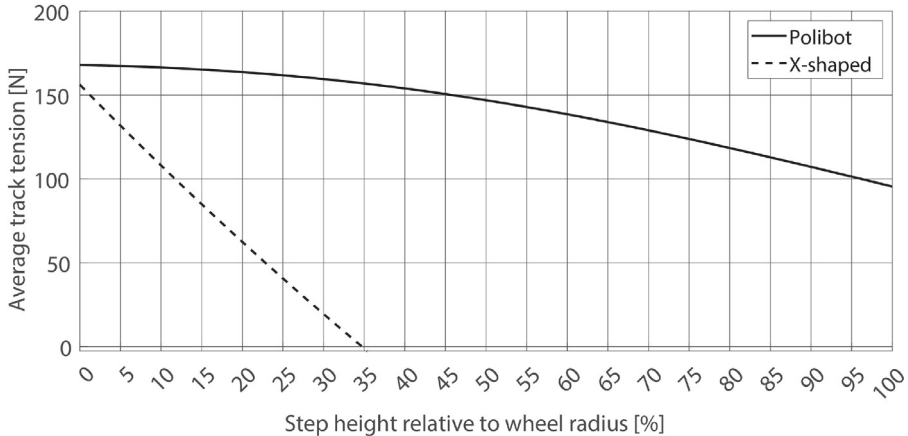


Fig. 21. Effect of obstacle height below the first road wheel on track tension: Polibot (black line) and X-shaped robot (black dashed line).

As a final remark, it should be noted that Polibot offers greater mechanical simplicity. In fact, the bioinspired suspension requires seven revolute joints and six rigid links per road wheel, which means that overall the robot of Fig. 19 would require twenty eight revolute joints and thirty links per track, against the nine joints and five links used by Polibot.

## 6. Conclusions

This paper presented a novel off-road tracked robot named Polibot with an innovative passively articulated suspension system, in which each road wheel is independently suspended to adapt to terrain irregularities and distribute pressure evenly in all conditions. The proposed architecture has greater mobility when compared with non-articulated robots or other passively articulated solutions, but it is still mechanically simpler than actively articulated suspensions.

A modeling tool for the inverse kinematics of the proposed design is also presented. The model is represented by a system of 21 equations that includes constraints and a quasi-static analysis. The unknowns of the problem are the seven degrees of freedom of the suspension and the fourteen unknown forces, including contact and internal forces.

The validation against experimental results shows good agreement with the results of the model, which is able to predict the system configuration given the terrain geometry. The model is also used to evaluate the impact of suspension design parameters and operating conditions, proving that it is a useful tool to optimise the current prototype of Polibot, or to design the future generations of the rover.

The current model will be further developed in future work to include a full dynamic analysis of the suspension and to account for the terramechanics at the track-ground interface. This tool can be implemented in the real robot for model-based control and estimation. As a further research, a model-based optimisation of Polibot design parameters can be developed.

## Declaration of competing interest

The authors declare that they have no known competing financial interests or personal relationships that could have appeared to influence the work reported in this paper.

## Data availability

Data will be made available on request.

## Acknowledgments

The financial support of the projects: Agricultural inTeroperabiLity and Analysis System (ATLAS), H2020 (Grant No. 857125), and multimodalsensing for individual plANT phenotyping in agrIculture robOtics (ANTONIO), ICTAGRI- FOOD COFUND (Grant No. 41946) is gratefully acknowledged.

## Appendix A. Geometric parameters of the suspension

Fig. A.1 presents a summary of the main geometric parameters of the bodies that make up the suspension.

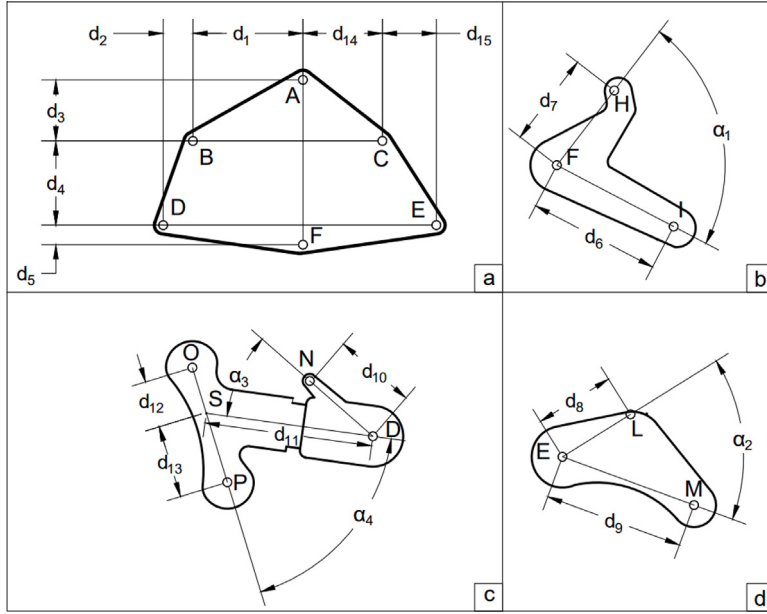


**Fig. A.1.** Geometry of the suspension bodies: (a) SF, (b) BRA and BFA, (c) FSA, (d) RSA.

## Appendix B. Derivation of wheel centers coordinates as a function of the degrees of freedom of the suspension

Given the geometry of the suspension (Figs. 5 and A.1), the X and Z coordinates of the wheel centers (P, K, I and M) can be expressed as a function of the degrees of freedom of Table 3 as follows:

$$X_P = X_A + (d_3 + d_4) \cdot \sin \theta - (d_1 + d_2) \cdot \cos \theta - d_{11} \cdot \sin (\theta_4 + \alpha_3) + d_{13} \cdot \sin (\theta_4 + \alpha_3 - \alpha_4) \quad (B.1)$$

$$X_K = X_A + (d_3 + d_4 + d_5) \cdot \sin \theta - d_6 \cdot \sin (\theta_2 + \alpha_1) \quad (B.2)$$

$$X_I = X_A + (d_3 + d_4 + d_5) \cdot \sin \theta + d_6 \cdot \sin \theta_1 \quad (B.3)$$

$$X_M = X_A + (d_3 + d_4) \cdot \sin \theta + (d_{14} + d_{15}) \cdot \cos \theta + d_9 \cdot \sin \theta_3 \quad (B.4)$$

$$Z_P = Z_A - (d_3 + d_4) \cdot \cos \theta_1 - (d_1 + d_2) \cdot \sin \theta_1 + d_{11} \cdot \cos (\theta_4 + \alpha_3) - d_{13} \cdot \cos (\theta_4 + \alpha_3 - \alpha_4) \quad (B.5)$$

$$Z_K = Z_A - (d_3 + d_4 + d_5) \cdot \cos \theta_1 + d_6 \cdot \cos (\theta_2 + \alpha_1) \quad (B.6)$$

$$Z_I = Z_A - (d_3 + d_4 + d_5) \cdot \cos \theta_1 - d_6 \cdot \cos \theta_1 \quad (B.7)$$

$$Z_M = Z_A - (d_3 + d_4) \cdot \cos \theta_1 + (d_{14} + d_{15}) \cdot \sin \theta_1 - d_9 \cdot \cos \theta_3 \quad (B.8)$$

## Appendix C. Derivation of length and direction of springs as a function of the degrees of freedom

The length of the three springs ( $S_1$ ,  $S_2$  and  $S_3$ ) can be obtained as a function of the degrees of freedom of Table 3 as follows:

$$L_1 = d_7 \cdot [\sin \theta_2 + \sin (\theta_1 + \alpha_1)] \quad (C.1)$$

$$L_2 = \sqrt{(X_L - X_C)^2 + (Z_L - Z_C)^2} \quad (C.2)$$

$$L_3 = \sqrt{(X_B - X_N)^2 + (Z_B - Z_N)^2} \quad (C.3)$$

where:

$$X_L - X_C = d_4 \cdot \sin \theta + d_{15} \cdot \cos \theta + d_8 \cdot \sin (\theta_3 + \alpha_2) \quad (C.4)$$

$$Z_L - Z_C = -d_4 \cdot \cos \theta + d_{15} \cdot \sin \theta - d_8 \cdot \cos (\theta_3 + \alpha_2) \quad (C.5)$$

$$X_B - X_N = d_2 \cdot \cos \theta - d_4 \cdot \sin \theta + d_{10} \cdot \sin \theta_4 \quad (\text{C.6})$$

$$Z_B - Z_N = d_2 \cdot \sin \theta + d_4 \cdot \cos \theta - d_{10} \cdot \cos \theta_4 \quad (\text{C.7})$$

For springs 2 and 3 it is also necessary to define their directions, indicated with  $\beta_2$  and  $\beta_3$  in Fig. 7:

$$\beta_2 = \text{atan2}(Z_C - Z_L, X_C - X_L) \quad (\text{C.8})$$

$$\beta_3 = \text{atan2}(Z_N - Z_B, X_N - X_B) \quad (\text{C.9})$$

where  $\text{atan2}$  is the four-quadrant inverse tangent.

#### Appendix D. Derivation of track length as a function of the degrees of freedom of the suspension

In this appendix, the expression of the length of the track as a function of the degrees of freedom of Table 3 is derived. The length can be calculated as the sum of line segments and arcs, where the track wraps around the wheels. For each wheel, the extension of the arc of contact with the track can be expressed as a function of the relative position of the following and precedent wheels. For example, the length of the section of the track that wraps around wheel 1 (Fig. D.2) delimited by the points  $Q_{12}$  and  $Q_{16}$  can be calculated as follows:

$$\bar{Q}_{12}Q_{16} = R_1 \cdot (2\pi + \delta_{fol} - \gamma_{fol} - \delta_{pre} - \gamma_{pre}) \quad (\text{D.1})$$

where  $R_1$  is the radius of wheel 1,  $\delta_{fol}$  is the orientation of the line  $\overline{AO}$  that points to the center of the following wheel,  $\delta_{pre}$  is the orientation of the line  $\overline{AM}$  that points to the center of the precedent wheel,  $\gamma_{fol}$  is the angle that defines the position of the tangency point  $Q_{12}$  with respect to  $\overline{AO}$ ,  $\gamma_{pre}$  is the angle that defines the position of the tangency point  $Q_{16}$  with respect to  $\overline{AM}$ . These angles can be computed as follows:

$$\delta_{fol} = \text{atan2}(Z_O - Z_A, X_O - X_A) \quad (\text{D.2})$$

$$\delta_{pre} = \text{atan2}(Z_M - Z_A, X_M - X_A) \quad (\text{D.3})$$

$$\gamma_{fol} = \arccos \frac{R_1 - R_2}{\overline{AO}} \quad (\text{D.4})$$

$$\gamma_{pre} = \arccos \frac{R_1 - R_6}{\overline{AM}} \quad (\text{D.5})$$

where  $\text{atan2}$  is the four-quadrant inverse tangent,  $R_2$  and  $R_6$  are the radii of wheels 2 and 6 respectively,  $\overline{AO}$  and  $\overline{AM}$  represent the length of the segment of the correspondent line.

The next entity required for the calculation of the track length is the line segment delimited by the two tangency points  $Q_{12}$  and  $Q_{21}$ . Its length can be computed as follows:

$$\overline{Q_{12}Q_{21}} = \sqrt{\overline{AO}^2 + (R_1 - R_2)^2} \quad (\text{D.6})$$

Finally, an expression for the overall track length can be derived from the generalisation of Eqs. (D.1) and (D.6)<sup>1 2</sup>:

$$L_{track} = \sum_{i=1}^6 R_i \cdot (2\pi + \delta_{fol,i} - \gamma_{fol,i} - \delta_{pre,i} - \gamma_{pre,i}) + \sqrt{\overline{C_i C_{i+1}}^2 + (R_i - R_{i+1})^2} \quad (\text{D.7})$$

where  $C_i$  is the center of the wheel  $i$  and  $R_i$  is the radius of the wheel  $i$ .

Given the geometry of the suspension, all the terms in (D.7) can be expressed as a function of the degrees of freedom of Table 3. The final track length expression is omitted for brevity. A numerical approach is adopted for the solution of the equation set (1)–(8), using the trust region algorithm. To this end, the problem can be formulated as:

$$F(x) = 0 \quad (\text{D.8})$$

where  $x$  is the array of unknowns and  $F$  is the array of equations. The trust region algorithm is based on Newton's method, with improved robustness in the case of starting point far from the solution or in case of singular Jacobian. It can be proved that the trust region sub-problem is given by:

$$\min_d \left[ \frac{1}{2} F(x_k)^T F(x_k) + d^T J(x_k)^T F(x_k) + \frac{1}{2} d^T J(x_k)^T J(x_k) d \right] \quad (\text{D.9})$$

where  $x_k$  is the array of variables at iteration  $k$ ,  $J$  is the Jacobian of equation (D.8) and  $d$  is the search direction (i.e. the quantity to add to  $x_k$  to obtain  $x_{k+1}$ ). For more details on trust region methods, the interested readers can refer to [22].

<sup>1</sup> For the formula of Eq. (D.7) to work,  $\delta_{pre}$  must be numerically greater than  $\delta_{fol}$  for all wheels. It may happen that this condition is not verified for some wheels. In those situations, it is sufficient to add  $2\pi$  to  $\delta_{pre}$ .

<sup>2</sup> For wheel 6,  $R_{i+1}$  is replaced by  $R_1$ .

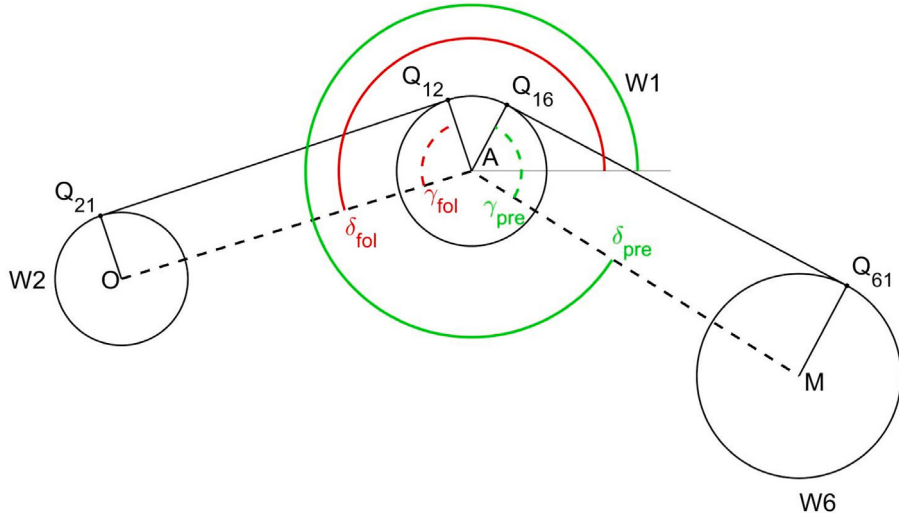


**Fig. D.2.** Geometric construction for the calculation of the length of the contact arc between track and wheel 1.

Finally, in the case of concave track profile, the formulas for the wheel on the outside of the track should be updated as follows, with respect to the same geometry of [Fig. D.2](#):

$$\gamma_{fol} = -\arccos \frac{R_1 + R_2}{AO} \quad (\text{D.10})$$

$$\gamma_{pre} = -\arccos \frac{R_1 + R_6}{AM} \quad (\text{D.11})$$

## Appendix E. Equilibrium equations

Referring to [Figs. 6](#) and [7](#), seven equilibrium equations can be obtained (global vertical forces, global moments around point P, moments on BRA around F, moments on BFA around F, moments on RSA around E and moments on FSA around D):

$$F_{tra} = F_{res} \quad (\text{E.1})$$

$$W = N_3 + N_4 + N_5 + N_6 \quad (\text{E.2})$$

$$N_4 \cdot (X_K - X_P) + N_5 \cdot (X_I - X_P) + N_6 \cdot (X_M - X_P) = W \cdot (X_G - X_P) \quad (\text{E.3})$$

$$N_5 \cdot d_6 \cdot \sin \theta_1 + F_{el,1} \cdot d_7 \cdot \cos(\theta_1 + \alpha_1) = 0 \quad (\text{E.4})$$

$$N_4 \cdot d_6 \cdot \sin(\theta_2 + \alpha_1) + F_{el,1} \cdot d_7 \cdot \cos \theta_2 = 0 \quad (\text{E.5})$$

$$N_6 \cdot d_9 \cdot \sin \theta_3 - T_1 \cdot (d_9 \cdot \cos \theta_3 + r_6) - F_{el,2} \cdot d_8 \cdot \cos(\theta_3 - \beta_2 + \alpha_2) + \\ - T_1 \cdot \cos \epsilon_{61} \cdot (Z_{Q_{61}} - Z_E) + T_1 \cdot \sin \epsilon_{61} \cdot (x_{Q_{61}} - x_E) = 0 \quad (\text{E.6})$$

$$N_3 \cdot [d_{11} \cdot \sin(\theta_4 + \alpha_3) - d_{13} \cdot \sin(\theta_4 + \alpha_3 - \alpha_4)] + \\ - F_{el,3} \cdot d_{10} \cdot \cos(\theta_4 - \beta_3) + \\ + T_2 \cdot [d_{13} \cdot \cos(\theta_4 + \alpha_3 - \alpha_4) - d_{11} \cdot \cos(\theta_4 + \alpha_3) + r_3] + \\ - T_2 \cdot \cos \epsilon_{21} \cdot (Z_{Q_{21}} - Z_D) - T_2 \cdot \sin \epsilon_{21} \cdot (x_D - x_{Q_{21}}) = 0 \quad (\text{E.7})$$

The directions of the elastic forces (indicated in [Fig. 7](#) with  $\beta_2$  and  $\beta_3$ ), are derived as a function of the degrees of freedom of [Table 3](#) in [Appendix C](#). The directions of the track tensions ( $\epsilon_{21}$  and  $\epsilon_{61}$ ) are derived in [Appendix D](#).

Finally, the last equation is given by the longitudinal equilibrium of the track element that exchanges forces with the ground:

$$F_{tra} = T_1 - T_2 \quad (\text{E.8})$$

## Appendix F. Analytical model for the X-shaped suspended robot

Referring to the suspension proposed by Sun et al. [16] and to the corresponding scheme of Fig. 19(b), the following equations can be written:

$$X_B = X_{CP_3} \quad (\text{F.1})$$

$$Z_B - r = 0 \quad (\text{F.2})$$

$$Z_C - r = 0 \quad (\text{F.3})$$

$$Z_D - r = 0 \quad (\text{F.4})$$

$$Z_E - r = 0 \quad (\text{F.5})$$

$$L_{track} = L_{nom} \quad (\text{F.6})$$

$$F_{z1} \cdot \cos(\theta) - F_{el,1} + T \cdot [\cos(\epsilon_{21} - \theta - \pi/2) - \sin(\theta)] = 0 \quad (\text{F.7})$$

$$F_{z2} \cdot \cos(\theta) - F_{el,2} = 0 \quad (\text{F.8})$$

$$F_{z3} \cdot \cos(\theta) - F_{el,3} = 0 \quad (\text{F.9})$$

$$F_{z4} \cdot \cos(\theta) - F_{el,4} + T \cdot [\cos(\pi/2 - \epsilon_{56} + \theta) + \sin(\theta)] = 0 \quad (\text{F.10})$$

$$F_{z1} + F_{z2} + F_{z3} + F_{z4} - Mg = 0 \quad (\text{F.11})$$

$$F_{z2} \cdot (X_C - X_B) + F_{z3} \cdot (X_D - X_B) + F_{z4} \cdot (X_E - X_B) - Mg \cdot (X_G - X_B) = 0 \quad (\text{F.12})$$

where (F.1) to (F.6) represent the constraint equations, which are the same used for Polibot model (Section 4.2), (F.7) to (F.10) are the equilibrium equations for each suspended wheel, (F.11) is the global equilibrium of external forces in the Z direction, (F.12) is the global equilibrium of external moments around point B. These 12 equations constitute a system in 12 unknowns: the position of the central frame ( $X_G$ ,  $Z_G$  and  $\theta$ ), the length of each elastic element ( $L_i$ , with  $i = 1, \dots, 4$ ), the normal reaction forces below each road wheel ( $F_{z,j}$ , with  $j = 1, \dots, 4$ ) and the average track tension  $T$ .

## References

- [1] J. Delmerico, S. Mintchev, A. Giusti, B. Gromov, K. Melo, T. Horvat, C. Cadena, M. Hutter, A. Ijspeert, D. Floreano, et al., The current state and future outlook of rescue robotics, *J. Field Robotics* 36 (7) (2019) 1171–1191.
- [2] F. Rubio, F. Valero, C. Llopis-Albert, A review of mobile robots: Concepts, methods, theoretical framework, and applications, *Int. J. Adv. Robot. Syst.* 16 (2) (2019).
- [3] A. Ugenti, F. Vulpi, R. Domínguez, F. Cordes, A. Milella, G. Reina, On the role of feature and signal selection for terrain learning in planetary exploration robots, *J. Field Robotics* 39 (4) (2022) 355–370.
- [4] A. Milella, G. Reina, M. Nielsen, A multi-sensor robotic platform for ground mapping and estimation beyond the visible spectrum, *Precis. Agric.* 20 (2) (2019) 423–444.
- [5] L. Bruzzone, G. Quaglia, Locomotion systems for ground mobile robots in unstructured environments, *Mech. Sci.* 3 (2) (2012) 49–62.
- [6] L. Bruzzone, S.E. Nodehi, P. Fanghella, Tracked locomotion systems for ground mobile robots: A review, *Machines* 10 (8) (2022) 648.
- [7] S. Morita, T. Hiramatsu, M. Niccolini, A. Argiolas, M. Ragaglia, Kinematic track modelling for fast multiple body dynamics simulation of tracked vehicle robot, in: 2018 23rd International Conference on Methods & Models in Automation & Robotics, MMAR, IEEE, 2018, pp. 910–915.
- [8] T. Haji, T. Kinugasa, K. Yoshida, H. Amano, K. Osuka, Experiment of maneuverability of flexible mono-tread mobile track and differential-type tracked vehicle, *Ind. Robot: Int. J.* (2010).
- [9] Z. Gong, F. Xie, X.-J. Liu, S. Shentu, Obstacle-crossing strategy and formation parameters optimization of a multi-tracked-mobile-robot system with a parallel manipulator, *Mech. Mach. Theory* 152 (2020) 103919.
- [10] Z. Luo, J. Shang, G. Wei, L. Ren, A reconfigurable hybrid wheel-track mobile robot based on Watt II six-bar linkage, *Mech. Mach. Theory* 128 (2018) 16–32.
- [11] W. Guo, J. Qiu, X. Xu, J. Wu, TALBOT: A track-leg transformable robot, *Sensors* 22 (4) (2022) 1470.
- [12] P.M. Moubarak, E.J. Alvarez, P. Ben-Tzvi, Reconfiguring a modular robot into a humanoid formation: A multi-body dynamic perspective on motion scheduling for modules and their assemblies, in: 2013 IEEE International Conference on Automation Science and Engineering, CASE, IEEE, 2013, pp. 687–692.
- [13] L. Bruzzone, M. Baggetta, S.E. Nodehi, P. Bilancia, P. Fanghella, Functional design of a hybrid leg-wheel-track ground mobile robot, *Machines* 9 (1) (2021).
- [14] W. Tao, Y. Ou, H. Feng, Research on dynamics and stability in the stairs-climbing of a tracked mobile robot, *Int. J. Adv. Robot. Syst.* 9 (4) (2012) 146.
- [15] J. Kim, J. Kim, D. Lee, Mobile robot with passively articulated driving tracks for high terrainability and maneuverability on unstructured rough terrain: Design, analysis, and performance evaluation, *J. Mech. Sci. Technol.* 32 (11) (2018) 5389–5400.
- [16] B. Sun, X. Jing, A tracked robot with novel bio-inspired passive “legs”, *Robot. Biomim.* 4 (1) (2017) 1–14.
- [17] G. Reina, M. Foglia, On the mobility of all-terrain rovers, *Ind. Robot: Int. J.* 40 (2) (2013) 121–131.
- [18] R. Galati, G. Reina, Terrain awareness using a tracked skid-steering vehicle with passive independent suspensions, *Front. Robot. AI* 6 (2019) 46.
- [19] W.G. Ata, A.M. Salem, Semi-active control of tracked vehicle suspension incorporating magnetorheological dampers, *Veh. Syst. Dyn.* 55 (5) (2017) 626–647.
- [20] T. Guo, J. Guo, B. Huang, H. Peng, Power consumption of tracked and wheeled small mobile robots on deformable terrains—model and experimental validation, *Mech. Mach. Theory* 133 (2019) 347–364.
- [21] A. Ugenti, R. Galati, G. Mantriota, G. Reina, Kinematic modelling of a high mobility tracked robot, in: The International Conference of IFToMM ITALY, Springer, 2022, pp. 37–44.
- [22] A.R. Conn, N.I. Gould, P.L. Toint, Trust-region methods, *Soc. Ind. Appl. Math.* (2000).